THE GIBBS PHENOMENON FOR RADIAL BASIS FUNCTIONS

BENGT FORNBERG* AND NATASHA FLYER†

Abstract. What is now known as the Gibbs phenomenon was first observed in the context of truncated Fourier expansions, but other versions of it arise also in situations such as truncated integral transforms and for different interpolation methods. Radial basis functions (RBF) is a modern interpolation technique which includes both splines and trigonometric interpolations as special cases in 1-D, and it generalizes these methodologies to scattered node layouts in any number of dimensions. We investigate here the Gibbs phenomenon for 1-D RBF interpolation, and find that it can differ also qualitatively from previously studied cases.

Key words. Radial basis functions, RBF, Gibbs phenomenon, interpolation.

1. Introduction. The best known version of the Gibbs phenomenon is the overshoot that arises when a discontinuous function is represented by a truncated set of Fourier expansion terms. A similar situation arises if a truncated Fourier expansion is instead obtained by means of interpolation on an equispaced grid. Figures 1.1a,b show more detailed pictures near a unit height jump in these two cases. In the limits of increasingly many terms and of increasingly high node densities, respectively, exact formulas for the peak heights are

$$\frac{1}{2} + \frac{1}{\pi}\int_0^\pi \frac{\sin\ t}{t} dt \approx 1.0895$$

and

$$\max_{0<\xi<1} \left\{ \frac{\sin\ \pi\xi}{\pi} \sum_{k=0}^{\infty} \frac{(-1)^k}{\xi - k} \right\} \approx 1.1411\ ,$$

i.e. the overshoots amount to approximately 8.95% and 14.11%, respectively, of the jump heights. Both of these cases are analyzed in [8], Section 2.4; see also [18], [19]. The amplitudes of successive oscillations decay in inverse proportion with the distance from the jump.

As Figure 1.1 (c) shows, the Gibbs phenomenon for splines differs from the previous cases especially in terms of how fast the oscillations decay. This is discussed further in Section 2. We then, in Section 3, generalize splines to what has become known as radial basis functions (RBF). This is a modern and extremely flexible interpolation method, which includes both splines and trigonometric interpolants in different 1-D special cases, but which applies immediately also when the data is given at scattered node locations in any number of space dimensions. The Gibbs phenomenon that arises for RBF interpolation has not been studied previously. We find in Section 4 that it can take quite different character in different situations. Section 5 contains some concluding remarks.

*University of Colorado, Department of Applied Mathematics, 526 UCB, Boulder, CO 80309, USA (fornberg@colorado.edu).

†National Center for Atmospheric Research, Division of Scientific Computing, 1850 Table Mesa Drive, Boulder, CO 80305, USA (flyer@ucar.edu)

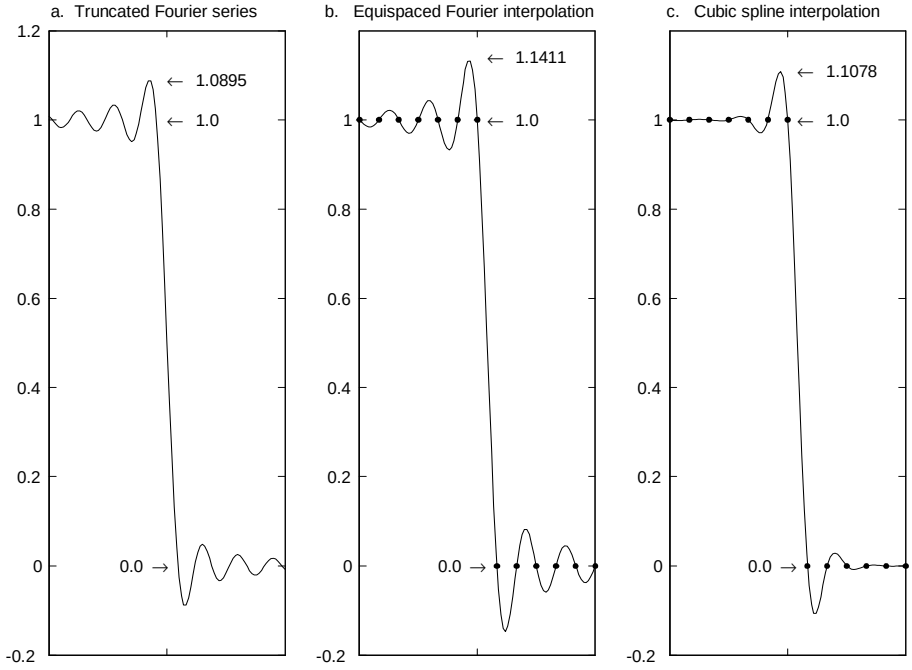

FIG. 1.1. *The Gibbs phenomenon for (a) truncated Fourier series, (b) equispaced Fourier interpolation, and (c) cubic spline interpolation. For (b) and (c), the nodes are located at the integers, with function value zero at positive integers, else one.*

2. The Gibbs phenomenon for spline interpolations. In the case of cubic splines, one can readily write down the cubic polynomials for each interval in closed form [9]. In the case shown in Figure 1.1c, the maximum appears on [-1,0], with the cubic over this interval given by

$$1 + (-\tfrac{3}{2} + \tfrac{\sqrt{3}}{2})x + (\tfrac{3}{2} - 3\tfrac{\sqrt{3}}{2})x^2 + (3 - 2\sqrt{3})x^3 \ .$$

The maximum value of $\frac{1}{6}(8 - 2\sqrt{2} - \sqrt{3} - \sqrt{6}) \approx 1.1078$ occurs at the location $x = \frac{1}{6}(-3 - \sqrt{3} + \sqrt{6}) \approx -0.3804$.

The cubic B-spline takes, at successive nodes, the values $\{0, \frac{1}{6}, \frac{2}{3}, \frac{1}{6}, 0\}$. Given that the B-spline expansion coefficients b_k for $k \geq 1$ in the case of the step data in Figure 1.1 (c) will need to satisfy the linear recursion relation

$$\frac{1}{6}b_{k-1} + \frac{2}{3}b_k + \frac{1}{6}b_{k+1} = 0$$

with characteristic equation $\frac{1}{6}r^2 + \frac{2}{3}r + \frac{1}{6} = 0$, it follows that the B-spline coefficients - and therefore the Gibbs oscillations - will decay for increasing $|k|$ at the exponential rate

$$|b_k| = O((2 - \sqrt{3})^{|k|}) \approx O(e^{-1.3170\,|k|}).$$

This fast rate may not be surprising given that the cubic spline, of all possible interpolants $s(x)$ to the given data, minimizes $\int_{-\infty}^{\infty}[s''(x)]^2 dx$. Persistent oscillations

Spline degree	Maximum value	Oscillation decay rate $O(e^{-\,c\,\lvert k\rvert})$; $c =$
3	1.1078	1.3170
5	1.1263	0.8426
7	1.1326	0.6250
9	1.1356	0.4976
11	1.1372	0.4136
⋮	⋮	⋮
21	1.1400	0.2247
⋮	⋮	⋮
∞	1.1411	0

TABLE 2.1
Trends in the Gibbs phenomenon for spline interpolation of increasing orders

cannot be present at increasing distances from the jump location because such would make this integral quantity large.

In the case of splines of higher orders, closed form expressions for the overshoot and for the decay rates become more involved, but the quantities are nevertheless easy to compute numerically. Table 2.1 summarizes some further cases. In the limit of increasing spline orders, we can see how the trigonometric interpolation case is recovered (as also follows from the fact that spline interpolants of increasing odd orders to cardinal data $s(x) = \begin{cases} 1 & \text{if } x{=}0 \\ 0 & \text{otherwise, when } x \in Z \end{cases}$ approach $\frac{\sin \pi x}{\pi x}$ uniformly in x; see for ex.[24]). The exponential coefficient decay is lost, and the slow algebraic rate has instead become dominant.

3. Radial basis functions. The RBF methodology was originated by Rolland Hardy around 1970 in connection with a cartography application that required multivariate scattered-node interpolation [17]. In a much noted 1982 survey [16], this approach, using a certain type of basis functions known as multiquadrics (MQ), was found to be the preferable one of about 30 then known methods (scoring the best in 13 out of 18 tests, and second best in 3 of the remaining 5 tests). Although unconditional non-singularity of the interpolation problem was known early in a very special case [2], it was the breakthrough discovery in 1986 of guaranteed nonsingularity also for MQs [22] which propelled the development of RBF into one of the most active areas in modern computational mathematics.

In the brief RBF introduction below (following a more extensive description in [10]), we first introduce RBF as a generalization of standard cubic splines to multiple dimensions. The types of RBF we are most interested in depend on a scalar *shape parameter* ε. The limit of $\varepsilon \to 0$ (basis functions becoming increasingly flat) is of special interest, since the accuracy then can become particularly high, with both polynomial and trigonometric interpolants arising as special cases [6], [9], [13], [14].

3.1. Introduction to RBF via cubic splines. A cubic spline is made up of a different cubic polynomial between each pair of adjacent node points (in 1-D), and it may at these node points feature a jump in the *third* derivative (i.e. the function, and its first two derivatives are continuous everywhere). The standard approach for computing the coefficients of the different cubics which form the spline requires only the solution of a tridiagonal linear system. If the spacing between the sample points is

h, it is well known that the size of the error, when interpolating smooth functions, will decrease like $O(h^4)$. It makes almost no difference in the algorithm if the nodes are not equally spaced. However, simple generalizations to more space dimensions have in the past been available only if the nodes are lined up in the coordinate directions.

Another way to approach the problem of finding the 1-D cubic spline (for now omitting to address the issue of end conditions) is the following: At each data location x_i, $i = 1, \ldots, n$, place a translate of the function $\phi(x) = |x|^3$, i.e. at x_i the function $\phi(x - x_i) = |x - x_i|^3$. We then ask if it is possible to form a linear combination of all these functions

$$s(x) = \sum_{i=1}^{n} \lambda_i \, \phi(x - x_i) \tag{3.1}$$

such that this takes the desired function values f_i at the data locations x_i, $i = 1, \ldots, n.$, i.e. such that $s(x_i) = f_i$ holds. This amounts to asking for the coefficients λ_i to satisfy a linear system of equations

$$\begin{bmatrix} \phi(x_1 - x_1) & \phi(x_1 - x_2) & \cdots & \phi(x_1 - x_n) \\ \phi(x_2 - x_1) & \phi(x_2 - x_2) & & \phi(x_2 - x_n) \\ \vdots & & & \vdots \\ \phi(x_n - x_1) & \phi(x_n - x_2) & \cdots & \phi(x_n - x_n) \end{bmatrix} \begin{bmatrix} \lambda_1 \\ \lambda_2 \\ \vdots \\ \lambda_n \end{bmatrix} = \begin{bmatrix} f_1 \\ f_2 \\ \vdots \\ f_n \end{bmatrix} . \tag{3.2}$$

Assuming that this system is non-singular, it can be solved for the coefficients λ_i. The interpolant $s(x)$, as given by (3.1), will then become a cubic function between the nodes and, at the nodes, have a jump in the third derivative. We have thus found another way to create an interpolating cubic spline. This time, we have arrived at a full linear system rather than a tridiagonal one. However, as we will see next, this formulation opens up powerful opportunities for generalizing the form of the interpolant, and also for extending the methodology to scattered data in any number of space dimensions.

3.2. Generalization to multiple dimensions. Figure 3.1a illustrates the RBF idea in 1-D. At each data location x_i, we have centered a translate of our symmetric function $\phi(x)$. In 2-D, as illustrated in Figure 3.1b, we instead use a *rotated* version of the same radial function. In d dimensions, we can write these rotated basis functions as $\phi(||\underline{x} - \underline{x}_i||)$, where $\|\cdot\|$ denotes the standard Euclidean norm. The form of the RBF interpolant and of the linear system that is to be solved has hardly changed from the 1-D case. Instead of (3.1) and (3.2), we now use as interpolant

$$s(\underline{x}) = \sum_{i=1}^{n} \lambda_i \, \phi(\|\underline{x} - \underline{x}_i\|) \tag{3.3}$$

with the collocation conditions

$$\begin{bmatrix} \phi(\|\underline{x}_1 - \underline{x}_1\|) & \phi(\|\underline{x}_1 - \underline{x}_2\|) & \cdots & \phi(\|\underline{x}_1 - \underline{x}_n\|) \\ \phi(\|\underline{x}_2 - \underline{x}_1\|) & \phi(\|\underline{x}_2 - \underline{x}_2\|) & & \phi(\|\underline{x}_2 - \underline{x}_n\|) \\ \vdots & & & \vdots \\ \phi(\|\underline{x}_n - \underline{x}_1\|) & \phi(\|\underline{x}_n - \underline{x}_2\|) & \cdots & \phi(\|\underline{x}_n - \underline{x}_n\|) \end{bmatrix} \begin{bmatrix} \lambda_1 \\ \lambda_2 \\ \vdots \\ \lambda_n \end{bmatrix} = \begin{bmatrix} f_1 \\ f_2 \\ \vdots \\ f_n \end{bmatrix} . \tag{3.4}$$

In particular, we note that the algebraic complexity of the interpolation problem has not increased with the number of dimensions - we will always end up with a square symmetric system of the same size as the number of data points. Cubic splines have thus been generalized to apply also to scattered data in any number of dimensions.

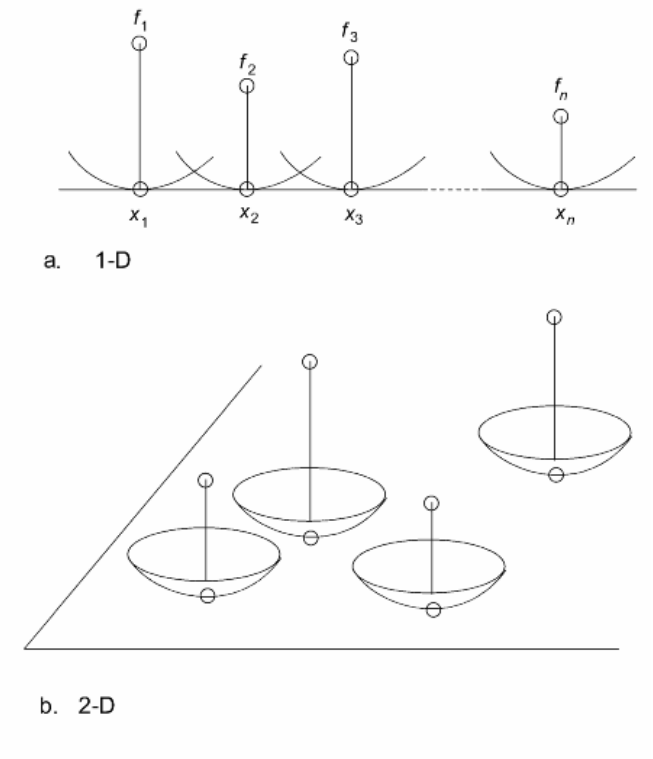

FIG. 3.1. *Illustration of the RBF concept in 1-D and in 2-D.*

3.3. Different types of radial functions. The error $O(h^4)$ for cubic splines in 1-D will become $O(h^6)$ in the case of quintic splines. And it falls to $O(h^2)$ for linear splines (corresponding to $\phi(x) = |x|$). In general, if we take the RBF approach as outlined above, and use $\phi(x) = |x|^{2m+1}$, the error will become $O(h^{2m+2})$ (even powers in $\phi(x)$ will not work; for ex. if $\phi(x) = x^2$, the interpolant (3.1) will reduce to a single quadratic polynomial, no matter the value of n, and attempting to interpolate more than three points will have to give rise to a singular system). The sizes of these errors correspond directly to which derivative of $\phi(x)$ is it that features a jump at the origin. This leads to the 'obvious' question: why not choose a $\phi(x)$ which is infinitely differentiable everywhere, such as $\phi(x) = \sqrt{1+x^2}$? This idea is an excellent one - and can be applied to good advantage in any number of dimensions. If we still ignore boundary issues (possibly leading to some counterpart of the Runge phenomenon for polynomials), the accuracy will become spectral: better than any polynomial order, and generally of the form $O(e^{-c\,n})$, where $c > 0$ and n is the number of points [26].

Table 3.1 lists a number of possible choices of radial functions, with illustrations in Figure 3.2. In the piecewise smooth category (where we so far have discussed only $\phi(r) = |r|^{2m+1}$), we include now also thin plate splines $\phi(r) = |r|^{2m} \ln |r|$. These are commonly used in 2-D, especially then with $m = 1$. Just like the natural cubic spline (i.e. with end conditions $s''(a) = s''(b) = 0$) minimizes $\int_a^b [s''(x)]^2 dx$ over all possible 1-D interpolants, the RBF interpolant using $\phi(r) = r^2 \log r$ achieves the equivalent minimization for 2-D scattered data [7].

The spectral accuracy noted above for smooth radial functions holds in any num-

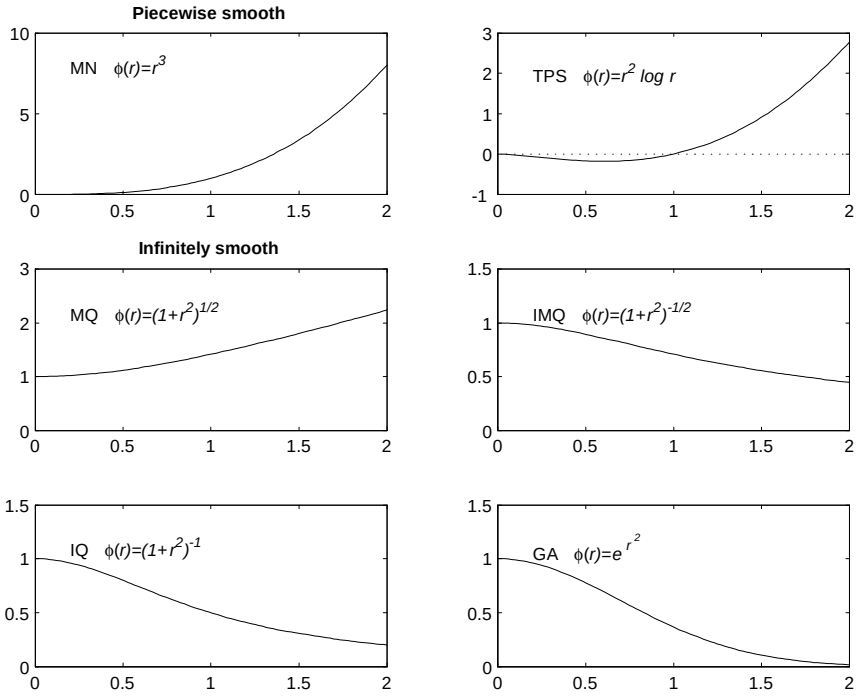

FIG. 3.2. *Illustrations of the six different radial functions in Table 3.1.*

ber of spatial dimensions. For the non-smooth RBF, the order accuracy actually improves with the number of dimensions, d. For example, for $\phi(r) = |r|^{2m+1}$ and for $\phi(r) = |r|^{2m} \ln |r|$, the order of accuracy becomes $O(h^{2m+1+d})$ and $O(h^{2m+d})$ respectively [23].

For the infinitely smooth RBF in Table 3.1, we have also introduced a *shape parameter*, which we denote by ε. For small values of ε, the basis functions become very flat, and for large values, they become sharply spiked (e.g. for IQ, IMQ, GA) or, in the case of MQ, it approaches the piecewise linear case. Table 3.1 also shows the Fourier transform of the radial functions (or generalized Fourier transform if the integral that defines the regular version would be divergent, cf. [1], [20], [21]; we use here the convention $u(x) = \frac{1}{2\pi} \int_{-\infty}^{\infty} \widehat{u}(\xi)\, e^{i\xi x} d\xi$, $\widehat{u}(\xi) = \int_{-\infty}^{\infty} u(x)\, e^{-i\xi x} dx$). The following are some key theorems regarding RBF interpolation. For proofs and further discussions, see for ex [3], [6], [10], [25]:

- All the smooth RBF choices listed in Table 3.1 will give coefficient matrices A in (3.4) which are nonsingular, i.e. there is a unique interpolant of the form (3.3) no matter how the (distinct) data points are scattered in any number of space dimensions. In the cases of IQ, IMQ and GA, the matrix is positive definite and, for MQ, it has one positive eigenvalue and the remaining ones all negative.
- Interpolation using MN and TPS can become singular in multi-dimensions. However, low degree polynomials can be added to the RBF interpolant to guarantee that the interpolation matrix is positive definite (a stronger condition than non-singularity). For example, for cubic RBF and TPS in d dimensions, this becomes the case if we use as interpolant $s(\underline{x}) = \sum_{k=1}^{d+1} \gamma_k p_k(\underline{x}) +$

Type of radial function			1-D **Fourier transform** $\widehat{\phi}(\xi)$
Piecewise smooth			
MN	monomial	$\lvert r\rvert^{2m+1}$	$\dfrac{(-1)^{m+1}(2m+1)!\sqrt{8\pi}}{\lvert\xi\rvert^{2m+2}}$
TPS	thin plate spline	$\lvert r\rvert^{2m}\ln\lvert r\rvert$	$\dfrac{(-1)^{m+1}(2m)!\sqrt{2\pi^3}}{\lvert\xi\rvert^{2m+1}}$
Infinitely smooth			
MQ	multiquadric	$\sqrt{1+(\varepsilon r)^2}$	$\dfrac{-2K_1\left(\frac{\lvert\xi\rvert}{\varepsilon}\right)}{\lvert\xi\rvert}$
IQ	inverse quadratic	$\dfrac{1}{1+(\varepsilon r)^2}$	$\dfrac{\pi}{\varepsilon}\,e^{-\frac{\lvert\xi\rvert}{\varepsilon}}$
IMQ	inverse MQ	$\dfrac{1}{\sqrt{1+(\varepsilon r)^2}}$	$\dfrac{1}{\varepsilon}K_0\left(\frac{\lvert\xi\rvert}{\varepsilon}\right)$
GA	Gaussian	$e^{-(\varepsilon r)^2}$	$\dfrac{\sqrt{\pi}}{\varepsilon}e^{-\xi^2/(4\varepsilon^2)}$
SH	Sech	$\mathrm{sech}(\varepsilon r)$	$\dfrac{\pi}{\varepsilon}\mathrm{sech}\left(\dfrac{\pi\xi}{2\varepsilon}\right)$

TABLE 3.1
Definition and Fourier transforms for some cases of radial functions

$\sum_{k=1}^{n}\lambda_k\ \phi(\|\underline{x}-\underline{x}_k\|)$ together with the constraints $\sum_{j=1}^{n}\lambda_j p_k(\underline{x}_j)=0, k=1,\ldots,d+1$. Here, $p_k(\underline{x})$ denotes a basis for polynomials of degree one in d dimensions, i.e. in the case of $d=3$ (with $x=(x_1,x_2,x_3)$), we have $p_1=1,\ p_2=x_1,\ p_3=x_2,\ p_4=x_3$.

- In 1-D, the RBF interpolant in the limit of $\varepsilon\to 0$ converges to Lagrange interpolation polynomial [6] (no matter how the distinct nodes are scattered).
- For 1-D periodic data, this same limit reproduces standard trigonometric interpolants (again, for all node distributions). For scattered nodes on a sphere, it reproduces a spherical harmonics interpolant [12].

4. The Gibbs phenomenon for RBF. Although the main point in using RBF is their flexibility in allowing smooth mesh-free interpolation of scattered data in any number of dimensions, we limit ourselves in this first study of the Gibbs phenomenon for RBF interpolants to 1-D unit-spaced data. For each of the radial functions in Table 3.1, we can introduce a 2π-periodic function

$$\Xi(\xi)=\sum_{k=-\infty}^{\infty}\phi(k)\ e^{i\,k\,\xi}=\sum_{j=-\infty}^{\infty}\widehat{\phi}(\xi+2\pi j). \tag{4.1}$$

The second sum above, following from Poisson's summation formula, will converge also in the cases where the first one diverges.

As a key step towards analyzing the Gibbs phenomenon, we consider cardinal data, defined at the integer lattice points as $f_0=1$ and $f_k=0$ at $x=k$ non-zero integer. It has previously been shown [4], [11] that the corresponding RBF expansion

coefficients then become

$$\lambda_k = \frac{1}{2\pi} \int_0^{2\pi} \frac{\cos k\xi}{\Xi(\xi)}\, d\xi \tag{4.2}$$

and the RBF cardinal interpolant becomes

$$s_C(x) = \frac{1}{2\pi} \int_{-\infty}^{\infty} \frac{\widehat{\phi}(\xi)\, \cos x\xi}{\Xi(\xi)}\, d\xi. \tag{4.3}$$

Derivations of these formulas are given in Appendix A. If we, in place of cardinal data, consider step (Gibbs-) data ($f_k = 1$ at $x = k$ non-positive integer and $f_k = 0$ at $x = k$ positive integer), adding translates of (4.3) gives the Gibbs interpolant as

$$s_G(x) = \sum_{j=0}^{\infty} s_C(x + j). \tag{4.4}$$

Substituting (4.3) into (4.4) leads to

$$s_G(x) = \frac{1}{2} - \frac{1}{4\pi} \int_{-\infty}^{\infty} \frac{\widehat{\phi}(\xi)}{\Xi(\xi)} \frac{\sin(x - \frac{1}{2})\xi}{\sin\frac{\xi}{2}}\, d\xi. \tag{4.5}$$

In contrast to (4.3) and (4.4), this simplified expression is only valid in cases for which $\Xi(\xi)\sin\frac{\xi}{2}$ is everywhere non-zero, (e.g. MN, TPS and MQ). The main task of the present study is to analyze and display $s_G(x)$. Our starting point will be to investigate how λ_k varies with k, as described by (4.2). The similarity between the integrals (4.2) and (4.3) will then permit the essential observations for λ_k to be carried over, first to $s_C(x)$ and then by (4.4) to $s_G(x)$. The next subsections describe these steps in more detail.

4.1. Analysis of cardinal expansion coefficients λ_k. Since this task was carried out in some detail in [11], we limit ourselves here to explaining the main ideas and results from that study. For some types of RBF, it turns out to be possible to extensively simplify the expressions that are obtained from combining the Fourier transforms from Table 3.1 with (4.1) and (4.2). For example:

Cubic RBF (MN with $j = 1$; same as cubic splines):

$$\lambda_0 = -4 + 3\sqrt{3}, \;\; \lambda_{\pm 1} = \tfrac{19}{2} - 6\sqrt{3} \;\text{ and }\; \lambda_{\pm k} = \tfrac{(-1)^k 3\sqrt{3}}{(2+\sqrt{3})^k}, \; k \geq 2$$

$$\text{IQ:} \;\; \lambda_k = \frac{(-1)^k \varepsilon \, \sinh(\frac{\pi}{\varepsilon})}{\pi^2} \int_0^{\pi} \frac{\cos\, k\omega}{\cosh(\omega/\varepsilon)} d\omega,$$

$$\text{GA:} \;\; \lambda_k = \frac{e^{(\varepsilon k)^2}}{2} \cdot \frac{\sum_{j=k}^{\infty} (-1)^j \, e^{-\varepsilon^2 (j+\frac{1}{2})^2}}{\sum_{j=0}^{\infty} (-1)^j (j + \frac{1}{2}) \, e^{-\varepsilon^2 (j+\frac{1}{2})^2}},$$

$$\text{SH:} \;\; \lambda_k = \frac{1}{\sum_{j=-\infty}^{\infty} (-1)^j \, \mathrm{sech}^2(\varepsilon j)} \cdot (-1)^k \, \mathrm{sech}(\varepsilon k).$$

Instead of pursuing more simplifications of this type, it turns out that we obtain more insights by evaluating the integral in (4.2) by means of Cauchy's theorem and the calculus of residues. The case of MQ is used below to illustrate this approach.

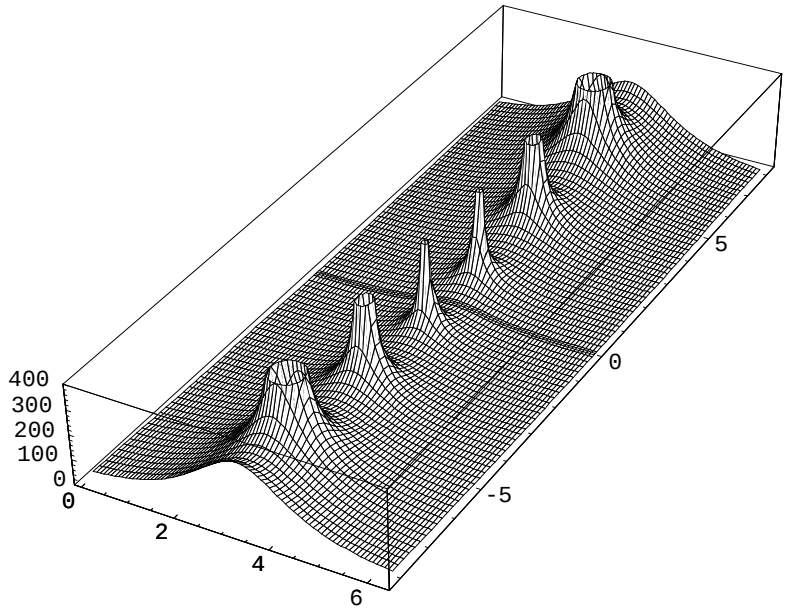

FIG. 4.1. *Magnitude of* $h(\xi)$*, as given by (4.6) over the domain* $0 \leq \mathrm{Re}\,\xi \leq 2\pi$, $-8 \leq \mathrm{Im}\,\xi \leq 8$.

4.1.1. Cardinal data expansion coefficients by contour integration. We consider MQ RBF and choose for simplicity $\varepsilon = 1$. The task becomes to evaluate

$$\lambda_k = -\frac{1}{4\pi} \int_0^{2\pi} h(\xi)\, e^{i\,k\,\xi} d\xi$$

where

$$h(\xi) = \frac{1}{\sum_{j=-\infty}^{\infty} \frac{K_1(|2\pi j+\xi|)}{|2\pi j+\xi|}}\ .$$

The function $h(\xi)$ is 2π-periodic, and can over $\xi \in [0, 2\pi]$ be written, without taking magnitudes, as

$$h(\xi) = \frac{1}{\sum_{j=0}^{\infty} \frac{K_1(2\pi j+\xi)}{2\pi j+\xi} \ + \ \sum_{j=1}^{\infty} \frac{K_1(2\pi j-\xi)}{2\pi j-\xi}}. \tag{4.6}$$

In this latter form, $h(\xi)$ can be extended as a single-valued analytic function throughout the strip $0 \leq \mathrm{Re}\,\xi \leq 2\pi$, $-\infty < \mathrm{Im}\,\xi < \infty$. Figure 4.1 illustrates the magnitude of this function, and Figure 4.2 shows its schematic character. We change the integration path as is indicated in Figure 4.2, and note that the two leading contributions to the integral, when k increases, will come from (i) the first pole and (ii) from the (non-cancelling) contributions from the vicinities of the branch points at $\xi = 0$ and $\xi = 2\pi$. Along the line $\xi = \pi + i\ t$, t real, the function $h(\xi)$ is purely real and $1/h(\xi)$ features decaying oscillations. The first pole of $h(\xi)$ appears near $\pi + 1.056109\ i$ and has a residue of approximately -34.866, thus contributing a term of $17.433\ (-1)^k\ e^{-1.056\,k}$ to λ_k. The singularity of $h(\xi)$ around the origin (repeated at $\xi = 2\pi$) comes from only one term in the denominator of (4.6), taking the form

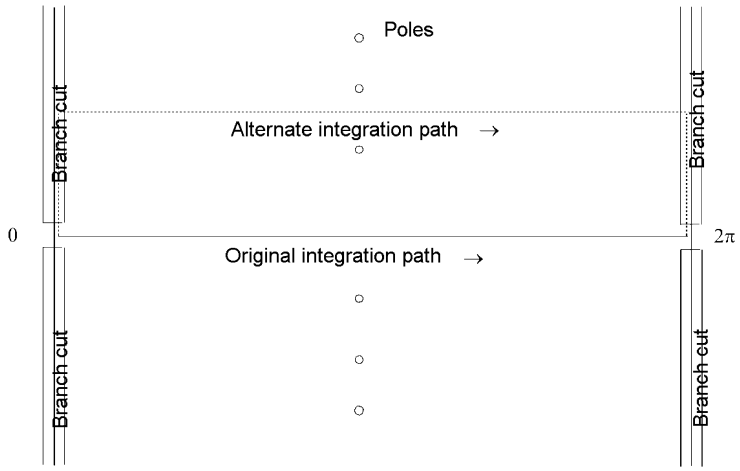

FIG. 4.2. *Character of the function $h(\xi)$ in the complex plane. The original and the modified integration paths are shown.*

$\frac{\xi}{K_1(\xi)} = \xi^2 + (\frac{1}{4} - \frac{\gamma}{2} + \frac{\ln 2}{2} - \frac{\ln \xi}{2})\xi^4 + \ldots$ The branch singularity is to leading order of the form $-\frac{1}{2}\xi^4 \ln \xi = -\frac{1}{2}\xi^4(\ln|\xi| + i\ \arg \xi)$ (and similarly around $\xi = 2\pi$). What does not cancel between the two sides of the contour but instead adds up (hence the factor 2 below) amounts to $2(-\frac{1}{4\pi}) \int_0^{i\cdot\{\text{some } \delta > 0\}} (-\frac{1}{2})\xi^4 i\ \frac{\pi}{2} e^{-ik\xi}\, d\xi$. Letting $\xi = it$ and noting that, as $k \to \infty$, we can change the upper integration limit to infinity, this simplifies to $-\frac{1}{8}\int_0^\infty t^4 e^{-kt} dt = -\frac{3}{k^5}$. For increasing k, we thus obtain

$$\lambda_k \quad \approx \underbrace{17.433\ (-1)^k\ e^{-1.056\ k} + \ldots}_{\text{exponential part}} \quad \underbrace{-\frac{3}{k^5} + \ldots}_{\text{algebraic part}} \tag{4.7}$$

Figures 4.3a,b compare, using log-linear and log-log scales respectively, the true values for $|\lambda_k|$ against the 2-term approximation in (4.7). The agreement is seen to be nearly perfect.

The same procedure as above can be carried through for any value of the shape parameter ε and also for all of the RBF types listed in Table 3.1. There will in every case be an exponential decay process, featuring oscillations in sign. It will depend on the regularity of $\widehat{\phi}(\xi)$ at $\xi = 0$ (branch point or not when continued to complex ξ) whether there will also be an algebraic non-oscillatory decay present. If this is present, it will dominate when k is sufficiently large. Given the expressions for $\widehat{\phi}(\xi)$ in Table 3.1, we can see that λ_k will decay exponentially for all k in the cases of MN (confirming what we obtained earlier when we considered MN splines in Section 2), GA and SH, whereas there will be a transition from exponential to algebraic decay in the cases of TPS, MQ, IQ and IMQ.

4.2. Cardinal data interpolants $s_C(x)$. The formulas for λ_k (4.2) and $s_C(x)$ (4.3) differ only in a few respects:

- A trivial multiplicative factor,
- The free parameter is called x instead of k (and we will consider it also for non-integer values),

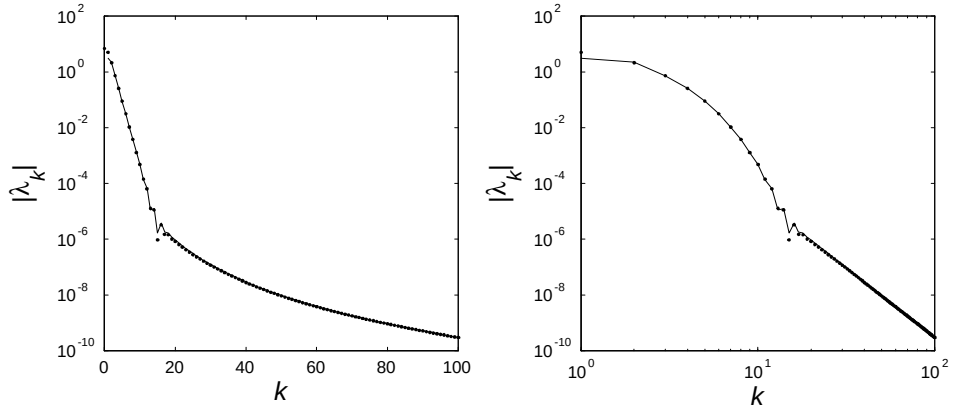

FIG. 4.3. *Comparison between correct values of $|\lambda_k|$ for MQ in 1-D, $\varepsilon = 1$ (dots) and the 2-term asymptotic formula (4.7) (solid line). The subplot to the left is log-linear and the one to the right of type log-log.*

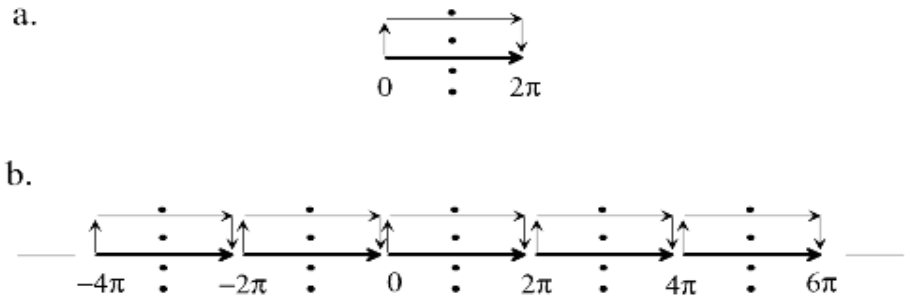

FIG. 4.4. *Original and modified integration contours for evaluating (a) the integral (4.2) for λ_k and (b) the integral (4.3) for $s_C(x)$.*

- There is an extra factor $\widehat{\phi}(\xi)$ in the numerator of (4.3),
- The integration interval is $[-\infty, \infty]$ instead of $[0, 2\pi]$.

In the same way as we deformed the contour for the integral (4.2), as was shown in Figure 4.2, and is again shown more schematically still in Figure 4.4a, we now deform the contour for (4.3) as is shown in Figure 4.4b. Since $\Xi(\xi)$ is 2π-periodic, the poles will in the two cases have the same imaginary parts, and therefore the exponential decay rates will be the same for $s_C(x)$ as was found for λ_k. The singularity at the origin will be cancelled by the factor $\widehat{\phi}(\xi)$ in the numerator of (4.3), but the contributions from other multiples of 2π will not be cancelled, so algebraic decay rates (if at all present) will also be the same (to leading order) for λ_k and $s_C(x)$.

We illustrate the general observations above with the case of IQ. In this case, it transpires that we can simplify (4.3) to

$$s_C(x) = \frac{\sinh \frac{2\pi}{\varepsilon} \sin \pi x}{\pi \varepsilon x (\cosh \frac{2\pi}{\varepsilon} - \cos 2\pi x)} \int_0^\pi \frac{\cos x\xi}{\cosh^2(\frac{\xi}{\varepsilon})}\, d\xi$$

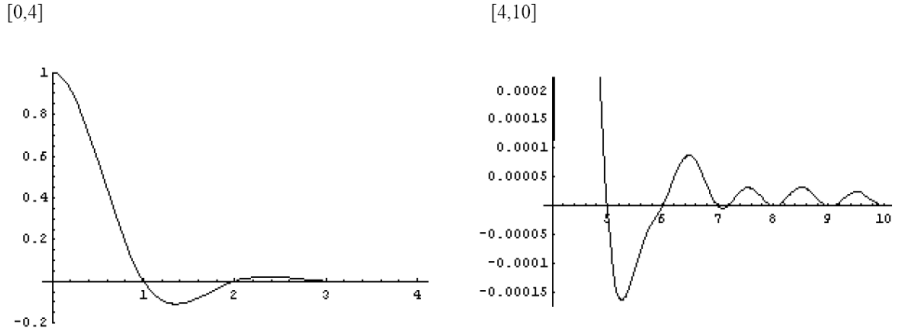

FIG. 4.5. *Cardinal interpolant $s_C(x)$ in the case of IQ, $\varepsilon = 1$, shown over the intervals (a) [0,4] and (b) [4,10].*

(now a finite integration interval and no Poisson sum). Figure 4.5 illustrates how this cardinal data interpolant at first decays in an oscillatory manner at an exponential rate, followed by algebraic decay without changes of sign, entirely as predicted by the general argument above.

4.3. Gibbs data interpolant $s_G(x)$. Considering the fast decay of cardinal RBF interpolants, it is clear that superposing translates of these according to (4.4) will give results for $s_G(x)$ which are qualitatively the same as those for the cardinal interpolant $s_C(x)$.

With help of the formulas (4.3), (4.4), or (4.5), one can readily compute the Gibbs interpolants for any radial function. Figures 4.6a-c show the Gibbs oscillations in a number of cases. In accordance with the analysis, we can note that the oscillations decay exponentially for all distances in cases when $\frac{1}{\hat{\phi}(\xi)}$ is analytic around the origin (here shown only in the case of GA), but otherwise there will at some distance be a transition to one-sided oscillations which decay at a slower algebraic rate. For the infinitely smooth RBF, it is also of interest to see how the Gibbs phenomenon varies with the shape parameter ε. As $\varepsilon \to 0$, the oscillations seen in Figure 4.7 c (MQ, $\varepsilon = 0.1$) increasingly resemble the trigonometric interpolation case shown in Figure 1.1b. The transition point between exponential and algebraic decay, visible around $x = 4$ in the case of $\varepsilon = 10$ (Figure 4.7a) and around $x = 16$ for $\varepsilon = 1$ (Figure 4.7b) has in the $\varepsilon = 0.1$ case moved too far out to be visible in computations carried out in standard 16-digit numerical precision. In this limit, the exponential decay has itself slowed up, and turned into the slow algebraic one of trigonometric interpolation.

4.4. Examples of Gibbs and Runge phenomena on a finite interval. In practical applications, RBF are almost always used on finite domains and with irregularly placed nodes. In contrast, analysis is most easily carried out - as we have done above - on equispaced infinite (or periodic) lattices. A key question that always must be asked following such analysis is to what extent the main observations will carry over to more practical situations. We will here focus this discussion on the test case of interpolating $f(x) = \arctan 20x$ over $x \in [-1, 1]$.

When using for example splines or finite elements, one can increase local resolution in areas of steep gradients by local insertion of additional nodes. Given that RBF also allow for arbitrary node locations, one might then attempt a similar strategy As Figure 4.8 shows, this can trigger oscillations away from the gradient area, that

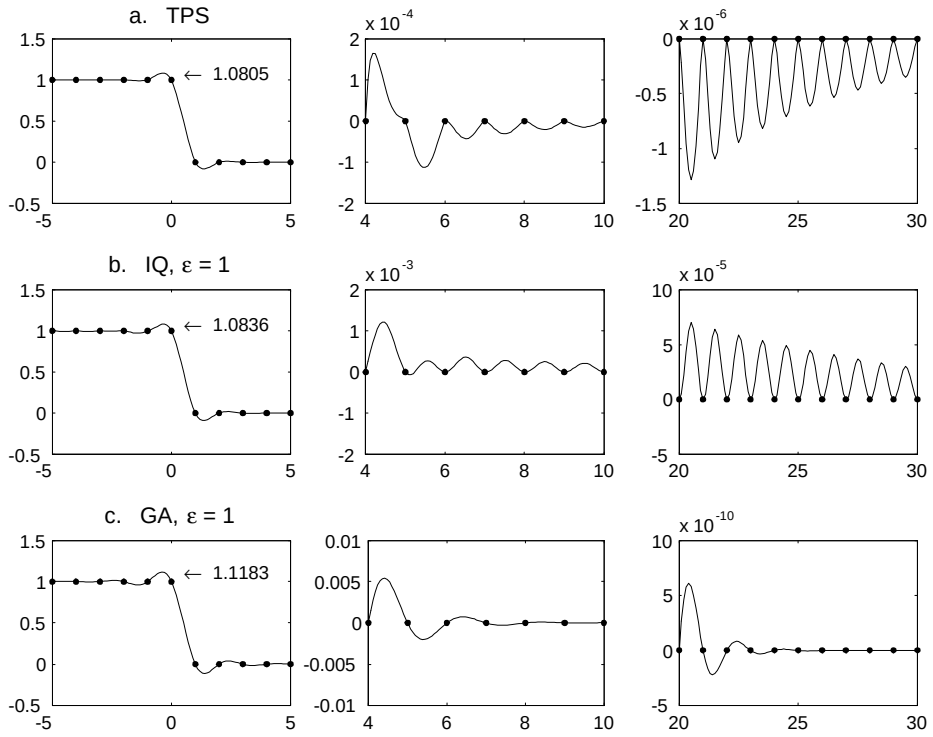

FIG. 4.6. *The Gibbs oscillations around a jump, and further out to the right, in the cases of (a) TPS, (b) IQ, ε=1, and (c) GA, ε=1.*

even might grow (rather than decay) with increasing distance. The issue is discussed in some detail in [15]. It is found there that the effect is better seen as an analog to the polynomial Runge phenomenon, and that care in selecting node locations *or* use of spatially variable shape parameter ε (using ε_k at node x_k) can not only overcome the oscillations, but in fact offer spectacular accuracies. This is illustrated in Figure 4.9. Bringing the nodes more smoothly towards the center (with the two center ones very close), together with a larger value of ε, reduces the error by two orders of magnitude. The new error pattern would appear to be related to the (surprising) one-sided Gibbs oscillation pattern that emerged from our analysis, and which was notable in the top two rows of subplots in Figure 4.7. Nearly two further orders of magnitude can be gained when allowing spatially variable ε. It can easily be verified that Chebyshev interpolation (polynomial interpolation at the locations of Chebyshev polynomial extrema; a standard procedure for non-periodic pseudospectral methods) will require $n = 170$ nodes to achieve the same $3 \cdot 10^{-5}$ accuracy as MQ RBF here did with $n = 10$ nodes.

The optimizations used to generate the data for Figure 4.9 were carried out using Matlab's *ga* (genetic algorithm) tool box. While this is not certain to give the true optima, nor is practical to use on a routine basis, it suffices very well for finding simple principles that characterize particularly accurate RBF approximations (such as choosing ε_k large where the nodes are close together).

The examples shown in Figure 4.9 were designed to illustrate how RBF can provide very high accuracy also in steep gradient situations. Several aspects of the

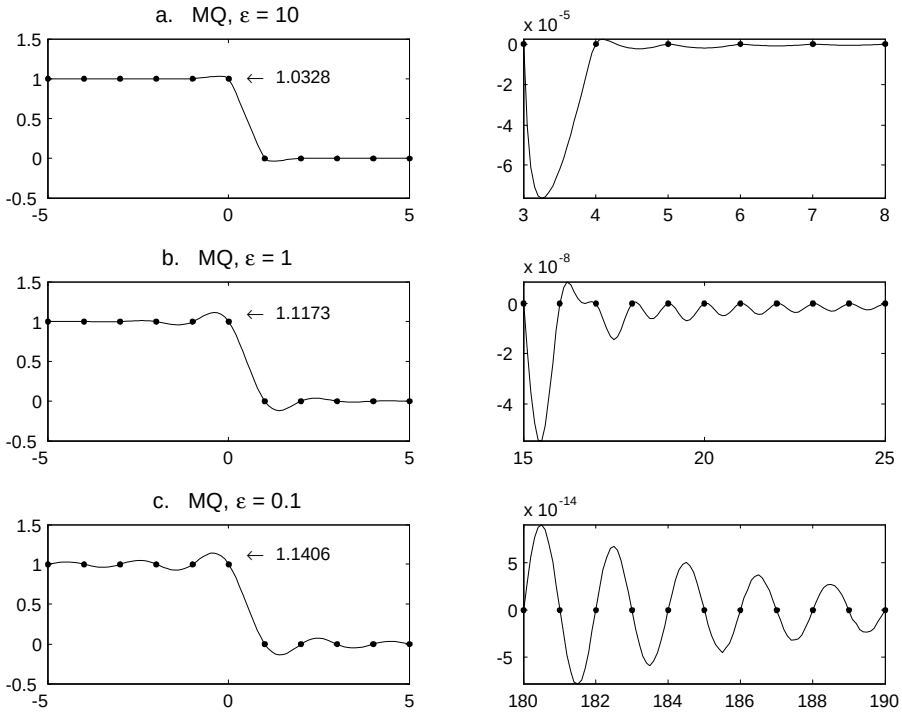

FIG. 4.7. *The Gibbs oscillations for MQ in the case of different values of the spape parameter (a) $\varepsilon = 10$, (b) $\varepsilon = 1$, and (c) $\varepsilon = 0.1$.*

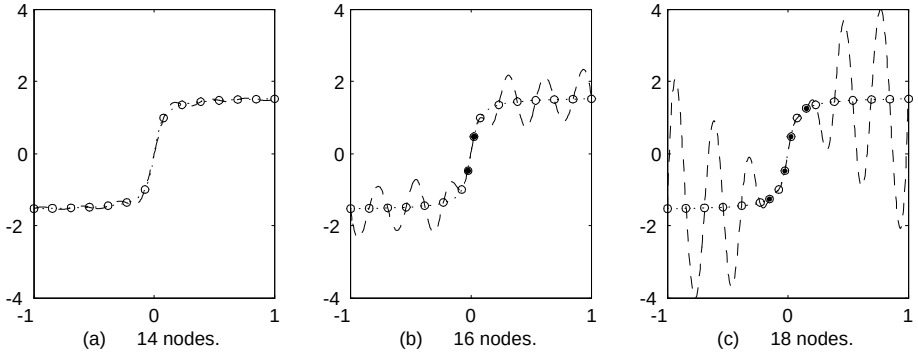

FIG. 4.8. *MQ $\varepsilon = 2$ interpolants to $f(x) = \arctan 20x$ over $[-1, 1]$: (a) 14 equispaced nodes, (b) with two extra nodes inserted near the center, and (c) with still two more nodes inserted.*

equispaced infinite lattice analysis for the Gibbs phenomenon can be observed, such as oscillations in some cases emanating from the 'jump', and in some cases the one-sided oscillation pattern. This simple example illustrates that opportunities exist - mostly still unexplored - to 'overcome' both Gibbs phenomena and related Runge phenomena.

5. Conclusions. There is much in common between the Gibbs phenomenon for RBF interpolation and for other interpolation types (such as splines and trigonometric

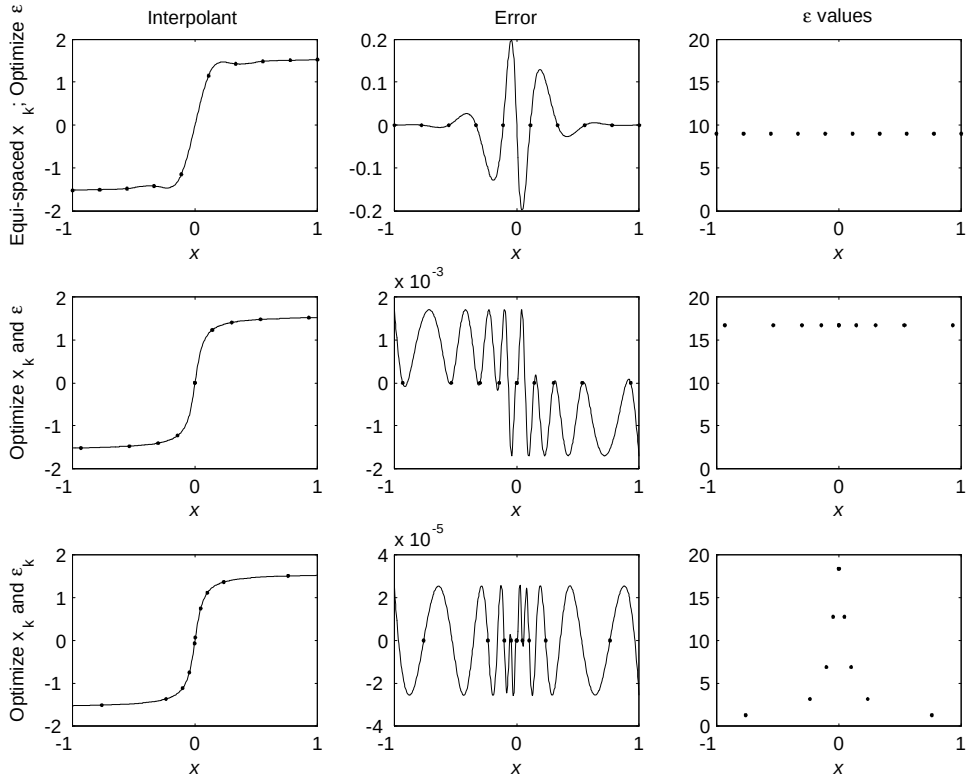

FIG. 4.9. *Ten-node MQ interpolations of* $f(x) = \arctan 20x$. *Top row: Equispaced nodes,* ε *(same at all nodes) optimized. Middle row: Node locations* x_k *and* ε *(same at all nodes) optimized. Bottom row: Both* x_k *and* ε_k *optimized.*

functions), but there are also significant differences, especially in terms of how the oscillations decay away from the jump. In RBF cases, both exponential and algebraic decays can be present and, if so, they will dominate at different distances from the jump discontinuity. Furthermore, oscillations without sign changes have not been seen previously in connection with the Gibbs phenomenon. The possibility of using a spatially variable shape parameter in RBF interpolation, as explored in [15], offers excellent opportunities for eliminating the adverse effects of the Gibbs phenomenon.

6. Acknowledgements. The National Center for Atmospheric Research (NCAR) is sponsored by the National Science Foundation. Natasha Flyer was supported by NSF Grant ATM-0620068. The work of Bengt Fornberg was supported by the NSF Grants DMS-0309803, DMS-0611681 and ATM-0620068. The present study builds on results for cardinal expansion coefficient decay rates, described in [11]. We acknowledge gratefully many discussions with Susan (Tyger) Hovde, Cécile Piret and Julia Zuev.

Appendix A

This appendix consists of three parts:

1. Derivation of (4.2)
2. Derivation of (4.3)

3. Verifying that the cardinal interpolant $s_C(x)$, as given by (4.3), indeed satisfies

$$s_C(n) = \begin{cases} 1 & n = 0 \\ 0 & n = \pm 1, \pm 2, \ldots \end{cases} . \tag{0.1}$$

1. Derivation of (4.2)

In terms of the 2π-periodic function

$$\Lambda(\xi) = \sum_{k=-\infty}^{\infty} \lambda_k \, e^{i\,k\,\xi}, \tag{0.2}$$

and $\Xi(\xi)$, as defined in (4.1), the cardinal coefficient relationship

$$\sum_{k=-\infty}^{\infty} \lambda_k \, \phi(n-k) = \begin{cases} 1 & n = 0 \\ 0 & n \neq 0, \; n \in Z \end{cases}$$

can be expressed as $\Lambda(\xi) \cdot \Xi(\xi) = 1$. Therefore, $\Lambda(\xi) = 1/\Xi(\xi)$. According to (0.2), the Fourier coefficients of this function are the expansion coefficients λ_k. Therefore, we obtain (4.2).

2. Derivation of (4.3)

The RBF cardinal interpolant becomes

$$\begin{aligned} s_C(x) &= \sum_{k=-\infty}^{\infty} \lambda_k \, \phi(x-k) \\ &= \frac{1}{(2\pi)^2} \sum_{k=-\infty}^{\infty} \left(\int_{-\pi}^{\pi} \frac{e^{i\,k\,\xi_1}}{\Xi(\xi_1)} d\xi_1 \right) \left(\int_{-\infty}^{\infty} \widehat{\phi}(\xi_2) \, e^{i\,x\,\xi_2 - i\,k\,\xi_2} d\xi_2 \right) \\ &= \frac{1}{(2\pi)^2} \int_{-\infty}^{\infty} \left(\underbrace{\int_{-\pi}^{\pi} \left(\sum_{k=-\infty}^{\infty} e^{i\,k\,(\xi_1 - \xi_2)} \right)}_{2\pi \, \delta(\xi_1 - \xi_2)} \frac{d\xi_1}{\Xi(\xi_1)} \right) \widehat{\phi}(\xi_2) \, e^{i\,x\,\xi_2} d\xi_2 \\ &= \frac{1}{2\pi} \int_{-\infty}^{\infty} \int_{-\infty}^{\infty} \delta(\xi_1 - \xi_2) \, \frac{\widehat{\phi}(\xi_2)}{\Xi(\xi_1)} \, e^{i\,x\,\xi_2} d\xi_1 d\xi_2 = \frac{1}{2\pi} \int_{-\infty}^{\infty} \frac{\widehat{\phi}(\xi)}{\Xi(\xi)} \, e^{i\,x\,\xi} d\xi \end{aligned}$$

3. Direct verification that $s_C(x)$ satisfies (0.1)

With $n \in Z$, we get

$$\begin{aligned} s_C(n) &= \frac{1}{2\pi} \int_{-\infty}^{\infty} \frac{\widehat{\phi}(\xi) \, e^{i\,n\,\xi}}{\sum_{j=-\infty}^{\infty} \widehat{\phi}(\xi + 2\pi j)} d\xi = \frac{1}{2\pi} \sum_{k=-\infty}^{\infty} \int_{-\pi}^{\pi} \frac{\widehat{\phi}(\xi + 2\pi k)}{\sum_{j=-\infty}^{\infty} \widehat{\phi}(\xi + 2\pi j)} \, e^{i\,n\,\xi} d\xi \\ &= \frac{1}{2\pi} \int_{-\pi}^{\pi} \underbrace{\left(\frac{\sum_{k=-\infty}^{\infty} \widehat{\phi}(\xi + 2\pi k)}{\sum_{j=-\infty}^{\infty} \widehat{\phi}(\xi + 2\pi j)} \right)}_{=1} e^{i\,n\,\xi} d\xi \\ &= \frac{1}{2\pi} \int_{-\pi}^{\pi} e^{i\,n\,\xi} d\xi = \begin{cases} 1 & n = 0 \\ 0 & n = \pm 1, \pm 2, \ldots \end{cases} . \end{aligned}$$

REFERENCES

[1] Arsac, J., Fourier Transforms and the Theory of Distributions, Prentice Hall, Englewood Cliffs, NJ, 1966.

[2] Bochner, S., Monotone Functionen, Stieltjes Integrale und harmonische Analyse, Math. Ann. 108 (1933), 378-410.

[3] Buhmann, M.D., Radial Basis Functions, Cambridge University Press, Cambridge (2003).

[4] M. D. Buhmann, Radial basis function interpolation on an infinite regular grid, in: Algorithms for Approximation II, eds. J. C. Mason and M. G. Cox, Chapman and Hall, 1990, pp. 47-61.

[5] Cheney, W. and Light, W., A Course in Approximation Theory, Brooks/Cole Publishing Company (2000).

[6] Driscoll, T.A. and Fornberg, B., Interpolation in the limit of increasingly flat radial basis functions, Comp. Math. with Applications 43 (2002), 413-422.

[7] Duchon, J. "Interpolation des fonctions de deux variables suivant le principe de la flexion des plaques minces." RAIRO Analyse Numérique 10, 5-12, 1976.

[8] Fornberg, B., A Practical Guide to Pseudospectral Methods, Cambridge University Press, Cambridge (1996).

[9] Fornberg, B., Driscoll, T.A., Wright, G. and Charles, R., Observations on the behavior of radial basis functions near boundaries, Comp. Math. with Applications 43 (2002), 473-490.

[10] Fornberg, B., and Flyer, N., Radial basis functions - Solving PDEs with spectral accuracy on irregular domains, Manuscript in preparation.

[11] Fornberg, B., Flyer, N., Hovde, S. and Piret, C., Localization properties of RBF expansions for cardinal interpolation. I. Equispaced nodes, Submitted to IMA Journal on Numerical Analysis.

[12] Fornberg, B. and Piret, C., A stable algorithm for radial basis functions on a sphere, submitted to SIAM J. Sci. Comp.

[13] Fornberg, B. and Wright, G., Stable computation of multiquadric interpolants for all values of the shape parameter, Comp. Math. with Applications 48 (2004), 853-867.

[14] Fornberg, B. Wright, G. and Larsson, E., Some observations regarding interpolants in the limit of flat radial basis functions, Comp. Math. with Applications 47 (2004), 37-55.

[15] Fornberg, B. and Zuev, J., The Runge phenomenon and spatially variable shape parameters in RBF interpolatiom, submitted to Comp. Math. with Applications.

[16] Franke, R., Scattered data interpolation: tests of some methods, Math. Comput. 38 (1982), 181-200.

[17] Hardy, R.L., Multiquadric equations of topography and other irregular surfaces, J. Geophy. Res., 76 (1971), 1905-1915.

[18] Helmberg, G., The Gibbs phenomenon for Fourier interpolation, J. Approx. Theory 78 (1994), 41-63.

[19] Jerri, A.J., The Gibbs Phenomenon in Fourier Analysis, Splines and Wavelet Approximations, Kluver Academic Publishers (1998).

[20] Jones, D.S., Generalized Functions, McGraw Hill, 1966.

[21] Lighthill, M.J., Fourier Analysis and Generalized Functions, Cambridge University Press, 1958.

[22] Micchelli, C.A., Interpolation of scattered data: distance matrices and conditionally positive functions, Constr. Approx. 2(1986), 11-22.

[23] Powell, M.J.D., The theory of radial basis function approximation in 1990, in Advances in Numerical Analysis, Vol. II: Wavelets, Subdivision Algorithms and Radial Functions, W. Light, ed., Oxford University Press, Oxford (1990), 105-210.

[24] Shim, H.-T. and Volkmer, H., On Gibbs phenomenon for wavelet expansions, J. of Approx. Theory 84 (1996), 74-95.

[25] Wendland, H., Scattered Data Approximation, Cambridge University Press, Cambridge (2005).

[26] Yoon, J., Spectral approximation orders of radial basis function interpolation on the Sobolev space, SIAM J. Math. Anal. 23 (2001), 946-958.